Three-dimensional double-diffusive Marangoni convection in a cubic cavity with horizontal temperature and concentration gradients

Jie-Min Zhan,[1,*] Zhi-Wu Chen,[1] Yok-Sheung Li,[2] and Yu-Hua Nie[3]
[1]*Department of Applied Mechanics and Engineering, Sun Yat-sen University, Guangzhou 510275, China*
[2]*Department of Civil & Structural Engineering, The Hong Kong Polytechnic University, Hong Kong, China*
[3]*South China Sea Branch, State Oceanic Administration, Guangzhou 510300, China*
(Received 3 August 2010; published 3 December 2010)

Three-dimensional double-diffusive Marangoni convection in a cubic cavity is studied in the present paper. Both the temperature and solute concentration gradients are applied horizontally. Direct numerical simulations are carried out for surface-tension Reynolds number $10 \leq \mathrm{Re} \leq 500$, surface-tension ratio $-2 \leq R_\sigma \leq 1$, and Lewis number $1 < \mathrm{Le} \leq 200$. Symmetry-breaking pitchfork bifurcation is observed, which does not exist in the pure thermocapillary case, and the flow field is essentially three dimensional. The evolution of the flow structure, as well as the dependence of the heat and mass transfer rates on the different parameters, is investigated systematically. The simulations are performed until the temporal chaotic flow regime is reached and an atypical bifurcation sequence is identified. Namely, as the thermal forcing of the system increases, the flow can undergo a reverse transition from a temporal chaotic to a steady state. Multiple solution branches exist in some parameter ranges, and these are depicted in terms of the heat and mass transfer rates. Corresponding two-dimensional simulations are also performed to clearly illustrate the deviations from the three-dimensional model. The onset of oscillatory flow from the quiescent equilibrium state is also considered. The present work intends to initiate the study of double-diffusive Marangoni convection in three-dimensional confined cavities with horizontal temperature and concentration gradients.

DOI: 10.1103/PhysRevE.82.066305 PACS number(s): 44.25.+f, 47.15.Fe, 47.20.Dr, 47.27.Cn

I. INTRODUCTION

Double-diffusive convection, which is driven by a combination of temperature and solute concentration gradients, has been the subject of intensive study. The system is known to display a wealth of dynamical behaviors whose properties depend on the direction and magnitude of the imposed gradients [1–3]. The earliest work was motivated by oceanographic applications and focused on situations in which both the temperature and concentration gradients are in the vertical direction. In contrast, in solidification convection is frequently induced by horizontal gradients [4], and this is the configuration of interest in the present study.

Both opposing (buoyancy ratio $N<0$) and augmenting ($N>0$) cases with parallel horizontal gradients have been studied experimentally [5,6], using electrochemical systems, and numerically [7,8]. The special case when the thermal and solutal buoyancy forces are equal and opposing ($N=-1$) is interesting since in this situation there exists a pure conduction state with linear profiles of temperature and concentration, and linear stability analysis can be used to identify the primary instability. This was first studied numerically by Krishnan [9] and was the topic of many more recent research efforts [10–13]. For a similar configuration it was shown very recently by Chen *et al.* [14] that the broken centrosymmetry of the system can lead to supercritical Hopf bifurcations near a series of codimension-2 bifurcation points.

In crystal growth and many other industrial processes, a liquid surface in contact with air is often present and Marangoni effects need to be taken into account. Like buoyancy force, liquid surface tension can also be simultaneously influenced by temperature and solute concentration. Double-diffusive Marangoni convection in a rectangular cavity with horizontal temperature and concentration gradients was first simulated by Bergman [15]. The most important result of this study is that, in the absence of buoyancy, convection may occur, even though the overall surface-tension difference along the free surface suggests stagnant fluid conditions (solutal to thermal Marangoni number ratio $R_\sigma=-1$). The nature of the first primary instability of the equilibrium had long time remained unknown, and very recently this was investigated systematically by Chen *et al.* [16]. The onset of both steady and oscillatory flows was studied by these authors, and further transitions to chaos were considered by Li *et al.* [17].

All the above mentioned studies were performed in two dimensions. Double-diffusive buoyancy convection in a cubical cavity with no-slip boundary conditions on all sides was first simulated by Sezai and Mohamad [18]. The parameter ranges $-2<N<0$, $10<\mathrm{Ra}<2\times10^5$, and $0.1<\mathrm{Le}<150$ were considered, where Ra is the thermal Rayleigh number and Le is the Lewis number, and complicated three-dimensional (3D) flow structures were obtained. The special opposing case $N=-1$ was studied in much more detail by Bergeon and Knobloch [19] using some bifurcation and stability analysis techniques. Sezai and Mohamad [18] focused on water-based solutions (Prandtl number $\mathrm{Pr}=10$), while the situation for a binary gas ($\mathrm{Pr}=0.71$) was studied by Verhaeghe *et al.* [20] using a lattice Boltzmann model. The influence of the horizontal diffusive walls on the three-dimensional flow was considered by Abidi *et al.* [21].

However, to the best of the authors' knowledge, three-dimensional analysis of double-diffusive Marangoni convec-

*Corresponding author; cejmzhan@gmail.com

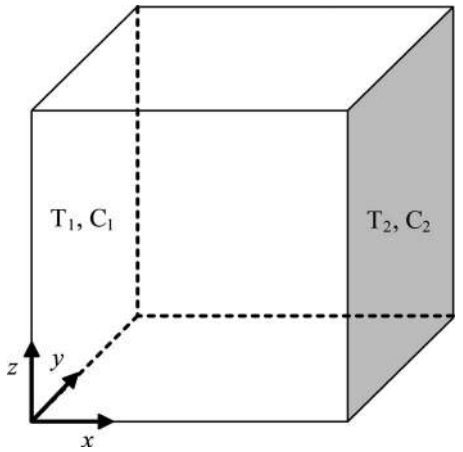

FIG. 1. Physical model and the coordinate system.

tion in a cubic cavity subjected to horizontal temperature and concentration gradients has not been reported. This provides direct motivation for the present work. We consider the same physical model as that of Sezai and Mohamad [18], except that the upper boundary is a free surface rather than a solid wall. The following parameter ranges are considered: $10 \leq \mathrm{Re} \leq 500$, $-2 \leq R_\sigma \leq 1$, and $1 < \mathrm{Le} \leq 200$. Each of these three parameters is varied in order to study the influences on the heat and mass transfer rates and on the three-dimensional flow structures. Direct numerical simulations are performed until the temporal chaotic regime is reached and an atypical bifurcation sequence is identified. Namely, a reverse transition from chaotic to steady flow is observed with the increase in Re. The onset of convection when $R_\sigma = -1$ is also considered. Section II provides a detailed description of the physical model studied. The numerical techniques used for simulations are explained in Sec. III. Then the results and discussions are given in Sec. IV, followed by some concluding remarks in Sec. V.

II. PROBLEM DEFINITION

The geometry under consideration is a cubic cavity filled with a binary fluid, with a nondeformable liquid-air surface on the top boundary (Fig. 1). Different temperatures and concentrations are specified at the left (T_1, C_1) and right (T_2, C_2) vertical walls, where $T_1 > T_2$ and $C_1 > C_2$, and zero heat and mass fluxes are imposed on the remaining boundaries. The no-slip boundary condition is adopted for all velocity components on the rigid walls, and on the top surface the Marangoni boundary condition is applied. The flow is assumed to be laminar and the binary fluid is assumed to be Newtonian and incompressible. The Boussinesq approximation is assumed to be valid except for the surface tension σ, which is allowed to vary linearly with the liquid temperature and solute concentration. Thus,

$$\sigma(T,C) = \sigma_0 - \gamma_T(T - T_0) - \gamma_C(C - C_0), \tag{1}$$

where $\sigma_0 = \sigma(T_0, C_0)$, $\gamma_T = -(\partial\sigma/\partial T)_C$, and $\gamma_C = -(\partial\sigma/\partial C)_T$. Thermophysical properties of the fluid are estimated at the reference temperature T_0 and concentration C_0, which are set to be equal to T_2 and C_2, respectively. For the majority of mixtures, liquid surface tension increases with the concentration of an inorganic solute and decreases for an organic solute. Since we are discussing double-diffusive convection in a broad sense and T and C are referred to components with higher and lower diffusivities, respectively, γ_T and γ_C can assume both positive and negative values. Buoyancy effects are neglected in the present study.

By choosing the cavity length L as the unit of length and υ/L as the unit of velocity, where υ denotes kinematic viscosity of the fluid, the nondimensionalized equations governing the conservations of mass, momenta, energy, and solute concentration can be written as

$$\frac{\partial u}{\partial x} + \frac{\partial v}{\partial y} + \frac{\partial w}{\partial z} = 0, \tag{2}$$

$$\frac{\partial u}{\partial t} + u\frac{\partial u}{\partial x} + v\frac{\partial u}{\partial y} + w\frac{\partial u}{\partial z} = -\frac{\partial P}{\partial x} + \left(\frac{\partial^2 u}{\partial x^2} + \frac{\partial^2 u}{\partial y^2} + \frac{\partial^2 u}{\partial z^2}\right), \tag{3}$$

$$\frac{\partial v}{\partial t} + u\frac{\partial v}{\partial x} + v\frac{\partial v}{\partial y} + w\frac{\partial v}{\partial z} = -\frac{\partial P}{\partial y} + \left(\frac{\partial^2 v}{\partial x^2} + \frac{\partial^2 v}{\partial y^2} + \frac{\partial^2 v}{\partial z^2}\right), \tag{4}$$

$$\frac{\partial w}{\partial t} + u\frac{\partial w}{\partial x} + v\frac{\partial w}{\partial y} + w\frac{\partial w}{\partial z} = -\frac{\partial P}{\partial z} + \left(\frac{\partial^2 w}{\partial x^2} + \frac{\partial^2 w}{\partial y^2} + \frac{\partial^2 w}{\partial z^2}\right), \tag{5}$$

$$\frac{\partial \theta}{\partial t} + u\frac{\partial \theta}{\partial x} + v\frac{\partial \theta}{\partial y} + w\frac{\partial \theta}{\partial z} = \frac{1}{\mathrm{Pr}}\left(\frac{\partial^2 \theta}{\partial x^2} + \frac{\partial^2 \theta}{\partial y^2} + \frac{\partial^2 \theta}{\partial z^2}\right), \tag{6}$$

$$\frac{\partial c}{\partial t} + u\frac{\partial c}{\partial x} + v\frac{\partial c}{\partial y} + w\frac{\partial c}{\partial z} = \frac{1}{\mathrm{Pr\,Le}}\left(\frac{\partial^2 c}{\partial x^2} + \frac{\partial^2 c}{\partial y^2} + \frac{\partial^2 c}{\partial z^2}\right), \tag{7}$$

together with boundary conditions

$$x = 0, \quad y \in [0,1], \quad z \in [0,1]: \quad u = v = w = 0, \quad \theta = c = 1, \tag{8}$$

$$x = 1, \quad y \in [0,1], \quad z \in [0,1]: \quad u = v = w = 0, \quad \theta = c = 0, \tag{9}$$

$$y = 0, \quad x \in [0,1], \quad z \in [0,1]: \quad u = v = w = 0,$$

$$\frac{\partial \theta}{\partial y} = \frac{\partial c}{\partial y} = 0, \tag{10}$$

$$y = 1, \quad x \in [0,1], \quad z \in [0,1]: \quad u = v = w = 0,$$

$$\frac{\partial \theta}{\partial y} = \frac{\partial c}{\partial y} = 0, \tag{11}$$

$$z = 0, \quad x \in [0,1], \quad y \in [0,1]: \quad u = v = w = 0,$$

TABLE I. Grid resolution test and comparison with the results of Sezai and Mohamad (S&M) [18] (Ra=10^7, Le=1, and Pr=0.71).

	Nu for $-1.5<N<-0.01$						
Grid	−0.01	−0.1	−0.2	−0.5	−0.8	−0.9	−1.5
40^3	17.20	16.72	16.15	14.08	10.77	8.79	14.08
50^3	16.64	16.20	15.68	13.74	10.61	8.69	13.74
60^3	16.48	16.06	15.54	13.65	10.56	8.67	13.65
70^3	16.41	15.99	15.48	13.60	10.54	8.66	13.60
80^3	16.36	15.94	15.44	13.58	10.53	8.65	13.58
S&M (80^3)	16.27	15.87	15.37	13.53	10.51	8.64	13.54

$$\frac{\partial \theta}{\partial z} = \frac{\partial c}{\partial z} = 0, \tag{12}$$

$$z = 1, \quad x \in [0,1], \quad y \in [0,1]: \quad w = 0, \quad \frac{\partial \theta}{\partial z} = \frac{\partial c}{\partial z} = 0, \tag{13}$$

$$\frac{\partial u}{\partial z} = -\mathrm{Re}\frac{\partial \theta}{\partial x} - \mathrm{Re}_S \frac{\partial c}{\partial x}, \tag{14}$$

$$\frac{\partial v}{\partial z} = -\mathrm{Re}\frac{\partial \theta}{\partial y} - \mathrm{Re}_S \frac{\partial c}{\partial y}. \tag{15}$$

There are four dimensionless parameters in the above system:

$$\mathrm{Pr} = \frac{\nu}{\alpha}, \quad \mathrm{Le} = \frac{\alpha}{D}, \quad \mathrm{Re} = \frac{\gamma_T \Delta T L}{\mu \nu}, \quad \mathrm{Re}_S = \frac{\gamma_C \Delta C L}{\mu \nu}, \tag{16}$$

which are, respectively, the Prandtl number, the Lewis number, and the thermal and solutal Reynolds numbers due to Marangoni effects. α denotes thermal diffusivity and D is the molecular diffusivity. Equations (14) and (15) are the so-called Marangoni boundary conditions, which equate the change in surface tension due to temperature and concentration variations across the surface to the shear stress experienced by the fluid at the surface. Re and Re_S are related to the classic thermal and solutal Marangoni numbers by Ma $=\mathrm{Re}\,\mathrm{Pr}$ and $\mathrm{Ma}_S = \mathrm{Re}_S\,\mathrm{Pr}$. In analogy with the buoyancy ratio N in double-diffusive buoyancy convection, the surface-tension ratio in double-diffusive Marangoni convection is defined as

$$R_\sigma = \frac{\mathrm{Ma}_S}{\mathrm{Ma}} = \frac{\gamma_C \Delta C}{\gamma_T \Delta T}. \tag{17}$$

A positive value of R_σ results in augmenting convection (cooperative Marangoni forces) and a negative value leads to opposing Marangoni forces. In the present study both augmenting and opposing cases are considered. The average heat and mass fluxes at the left vertical wall are given by the Nusselt and Sherwood numbers as

$$\mathrm{Nu} = \int_0^1 \int_0^1 \left| \frac{\partial \theta}{\partial x} \right|_{x=0} dydz, \tag{18}$$

$$\mathrm{Sh} = \int_0^1 \int_0^1 \left| \frac{\partial c}{\partial x} \right|_{x=0} dydz. \tag{19}$$

III. NUMERICAL METHOD

Equations (2)–(7) together with the boundary conditions (8)–(15) are discretized using nonuniform control volumes. Finer grids cluster near the boundaries in order to improve the numerical accuracy. Colocated variable arrangement is used and the SIMPLE algorithm is adopted to couple momentum and continuity equations. In searching for steady-state flow, initially very large time step is used for fast convergence. For cases where convergent steady solutions cannot be obtained small time steps are used to detect possible unsteady behavior. The time stepping is realized by the second-order implicit three-time level scheme. Details of the implementation of the numerical procedures can be found in work of Ferziger and Peric [22].

The two-dimensional (2D) version of the code has been carefully verified and successfully used to study the onset and further transitions of Marangoni convection [16,17]. Due to the absence of three-dimensional numerical results for double-diffusive Marangoni flow, we validate our 3D code by the buoyancy flow data of Sezai and Mohamad [18], where the counterpart problem is considered. Table I shows the Nusselt number for different grid resolutions and gives a comparison with that of Sezai and Mohamad [18] obtained with 80^3 nonuniform grids for Ra=10^7, Le=1, Pr=0.71, and different opposing buoyancy ratios. It can be seen that our results produced by the grid 80^3 agree very well with those by Sezai and Mohamad [18]. The maximum difference for all the buoyancy ratios considered is less than 0.6%. Also, the results by the grid 60^3 agree within 0.8% of those by the grid 80^3. To strike a balance between numerical accuracy and efficiency, the grid 60^3 is adopted for the present 3D study.

IV. RESULTS AND DISCUSSIONS

In the present study we investigate a moderate Prandtl number fluid, Pr=5. The development of 3D flow structures,

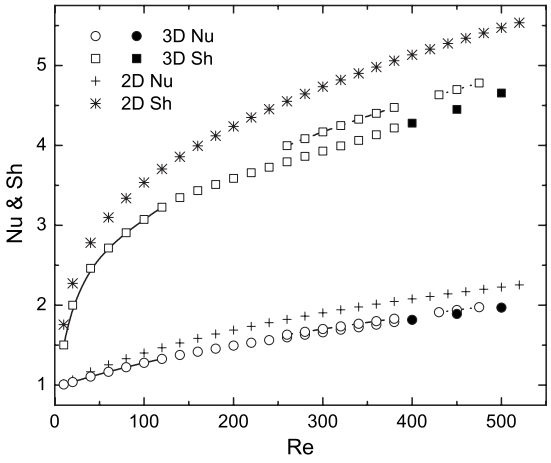

FIG. 2. Variations of Nu and Sh with the increase in Re for $R_\sigma=-0.5$ and Le=10. The solid circle and square points denote time averages of oscillatory flow results, while the others represent steady flow results. The steady 3D results connected by solid, dashed, and dotted lines represent two-roll, four-roll, and six-roll symmetric solutions, respectively, while those scattered points represent two-roll asymmetric solutions.

as well as the heat and mass transfer rates, is investigated as each of the parameters Re, R_σ, and Le varies. The effects of initial conditions on the resulting flow structures have also been investigated. For this purpose mainly three procedures have been used. In the first case the diffusive solution is used as the initial condition for all the calculations: temperature and concentration decrease linearly from 1 at the left vertical wall to zero at the right vertical wall and the velocities are all zero. In the second case the all-zero field is used as the initial condition for all the calculations: temperature, concentration, and all the velocity components are initially set to zero. In the third case a continuation type of procedure is used, where one of the parameters is increased in steps using the current solution as the initial condition for the next step. The sequence is then traversed backward by starting from the maximum value of the parameter until the initial value is reached. The resulting solution branches of Nu and Sh have been constructed and the deviations from the 2D model are illustrated. However, no attempt was made to uncover all possible bifurcating branches or to find out the mechanisms by which bifurcating solutions lose or gain stability.

A. Influence of Re

The influences of Re are summarized in Fig. 2 for $R_\sigma=-0.5$ and Le=10. In addition to the 3D solutions, 2D results are also provided to clearly depict their deviations. Up to Re=500, while the 2D results always correspond to steady-state flows, the 3D results consist of four different steady flow branches, one oscillatory flow branch and two different chaotic regimes (not plotted in Fig. 2). The evolution of the flow field is detailed below.

At Re=10 the flow, temperature, and concentration fields are shown in Fig. 3. The flow on the upper surface is almost parallel to the x axis and the whole flow field consists of a primary vortex, whose axis of rotation is parallel to the y axis. Furthermore, the flow field is symmetric with respect to the vertical plane $y=0.5$ (back-front symmetric). This is apparent when considering the geometry of the physical model and the boundary conditions imposed. Even at this small Reynolds number the three-dimensional nature of the flow is obvious, as can be seen from the stream slice on the mid-y-z plane ($x=0.5$) in Fig. 3(b). The isosurfaces of the temperature field are almost parallel to the left and right vertical walls, while those of the concentration field are much more distorted. It can be seen that, on the upper surface, the temperature gradient in the x direction is dominant over that of the concentration gradient for most part of the surface, and it is only near the right vertical wall that the concentration gradient is dominant. This explains the flow directions on the top surface [Fig. 3(a)].

As Re increases the flow on the upper surface diverges toward the back and front sidewalls and two secondary counter-rotating vortices develop on the mid-y-z plane. This is shown in Fig. 4 for Re=120. The flow structures are still back-front symmetric and we refer to this solution as the two-roll symmetric solution. The hollow square and circle points in Fig. 2 connected by solid lines represent this solution branch. Due to the increased intensity of the primary vortex, the isosurfaces of the temperature field are now more distorted than those in Fig. 3(c). In order to see through the volume we plot in Fig. 4(d) the contour slices, rather than the isosurfaces, of the concentration field. It can be seen that boundary layer forms near the left and right vertical walls. While the contour lines on the upper surface in Fig. 3(d) are shifted toward the right vertical wall, those in Fig. 4(d) are clearly deflected toward the left. This is because relatively fresh water has been brought from near the right vertical wall to below the top surface, creating adverse horizontal concentration gradient there. On the top surface, from the temperature and concentration gradients in the y direction it can be inferred that the two secondary vortices [Fig. 4(b)] are driven by solutal Marangoni effect.

When Re is increased from 120 to 140 a bifurcation is encountered and the back-front symmetry of the solution is broken. The asymmetric solution is presented in Fig. 5 for Re=200. The secondary flow on the mid-y-z plane no longer consists of two symmetric vortices, but has an asymmetric pattern, with the dominant vortex on the left side and the other limited to the upper-right corner of this cross section. Depending on the initial condition, another asymmetric flow pattern can be obtained, as presented in Fig. 6, which corresponds to exactly the same heat and mass transfer rates as those of Fig. 5. In fact, there is no physical reason why the dominant vortex is on the left- or right-hand side of this cross section, where both possibilities are equal, i.e., pitchfork bifurcation. That the figures show a preferred bias can be explained by numerical errors, which perturb the dominant flow to a certain side. The resulting two-roll asymmetric solution branch is denoted by the scattered hollow square and circle points in Fig. 2. We also performed corresponding simulations in the absence of solutal Marangoni force ($R_\sigma=0$) and no pitchfork bifurcation was observed. The flow is always back-front symmetric, which is in agreement with the study of Sass *et al.* [23]. Thus, it might be concluded that the pitchfork bifurcation is due to the existence of a solute com-

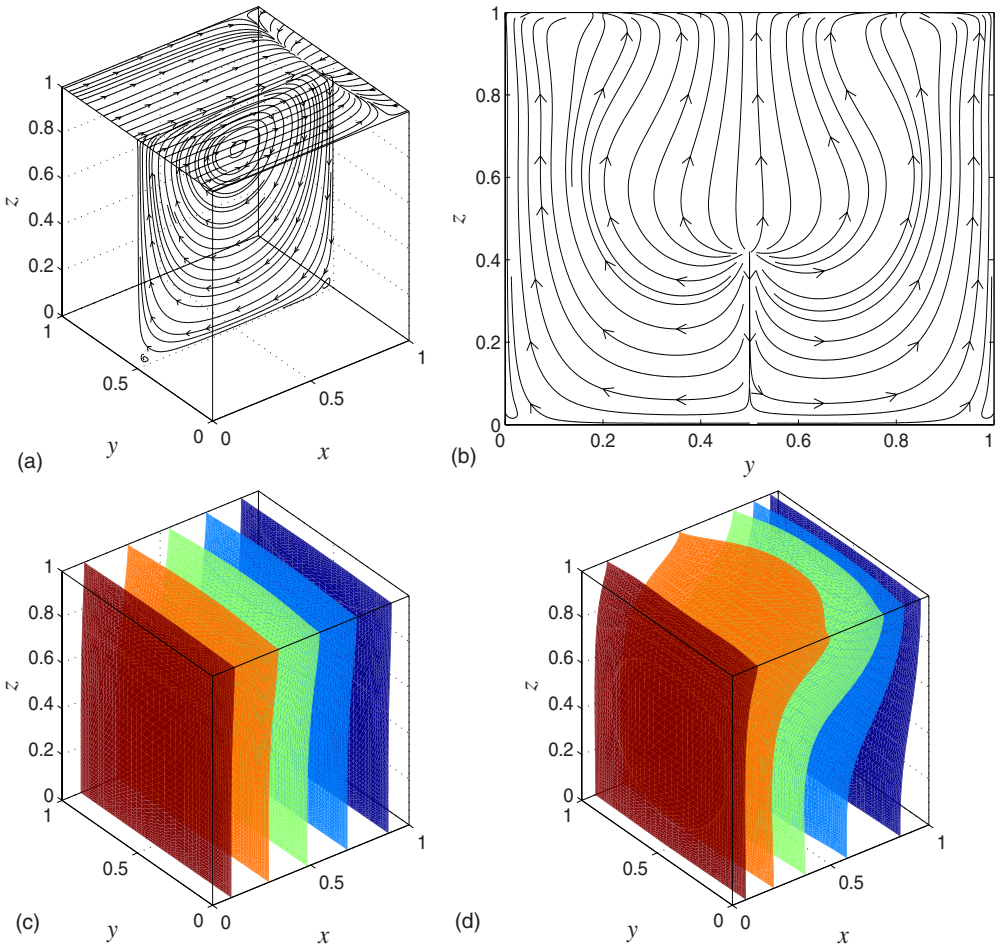

FIG. 3. (Color online) Re=10, R_σ=−0.5, and Le=10: (a) stream slices on the mid-x-z and the top x-y planes, (b) stream slice on the mid-y-z plane, (c) isosurfaces of the temperature field, and (d) isosurfaces of the concentration field. The values of 0.1, 0.3, 0.5, 0.7, and 0.9 are used for contours in both (c) and (d).

ponent, which diffuses much slower than the heat does.

In addition to the asymmetric secondary flow, one more important feature of Fig. 5 is that on the mid-x-z plane a solute-rich fluid core has developed below the upper surface [Fig. 5(d)]. As Re increases this fluid core further develops, and at Re=400 the two-roll asymmetric flow becomes oscillatory, as can be seen from the temporal responses of $u(0.5,0.5,1)$ and $v(0.5,0.5,1)$ shown in Fig. 7. The y velocity component has a much larger oscillation amplitude than that of the x component. The onset of oscillatory flow may be explained as follows. A disturbance that takes a fluid parcel from the interior to the free surface simultaneously creates a solute-rich spot due to the solute concentration distribution just described. Thus, surface tension is increased locally pulling surface fluid in and then back into the interior by continuity. Hence, the perturbation triggers a restoring mechanism conducive to overstability, and an oscillatory wavelike motion develops. The present oscillatory flow is stable up to Re=500, which is the maximum Re value considered in the present study. Since 3D oscillatory flow simulation is very time consuming, we did not continue the simulation much further. The oscillatory solution branch is denoted by the scattered solid square and circle points in Fig. 2.

For low Re values, using either the all-zero field or the diffusive solution as the initial condition leads to the two-roll symmetric solution, and then the above-mentioned bifurcation sequence is obtained by the continuation type of procedure using the current result as the initial field for the next run. When the diffusive solution is used as the initial condition for $260 \leq \mathrm{Re} \leq 380$ another steady solution branch can be obtained, as denoted by the hollow square and circle points connected by dashed lines in Fig. 2. The flow field at Re=340 is shown in Fig. 8. Back-front symmetry is regained and the secondary flow on the mid-y-z plane consists of two pairs of counter-rotating vortices. We refer to this solution as the four-roll symmetric solution. It is more efficient in heat and mass transfers than the two-roll asymmetric solution coexisting in the same parameter range (Fig. 2).

When Re is increased from 380 to 400 the solution becomes temporal chaotic, as can be seen from the temporal responses of $u(0.5,0.5,1)$ and $v(0.5,0.5,1)$ shown in Fig. 9(a). The correlation dimension [24] is adopted for computing the fractal dimension d of the corresponding strange attractor and this gives d=2.52. Thus, indeed the time series shown in Fig. 9(a) correspond to deterministic chaos rather than random signals. The snapshot of the flow field on the mid-y-z plane is shown in Fig. 9(b). It is still quite organized

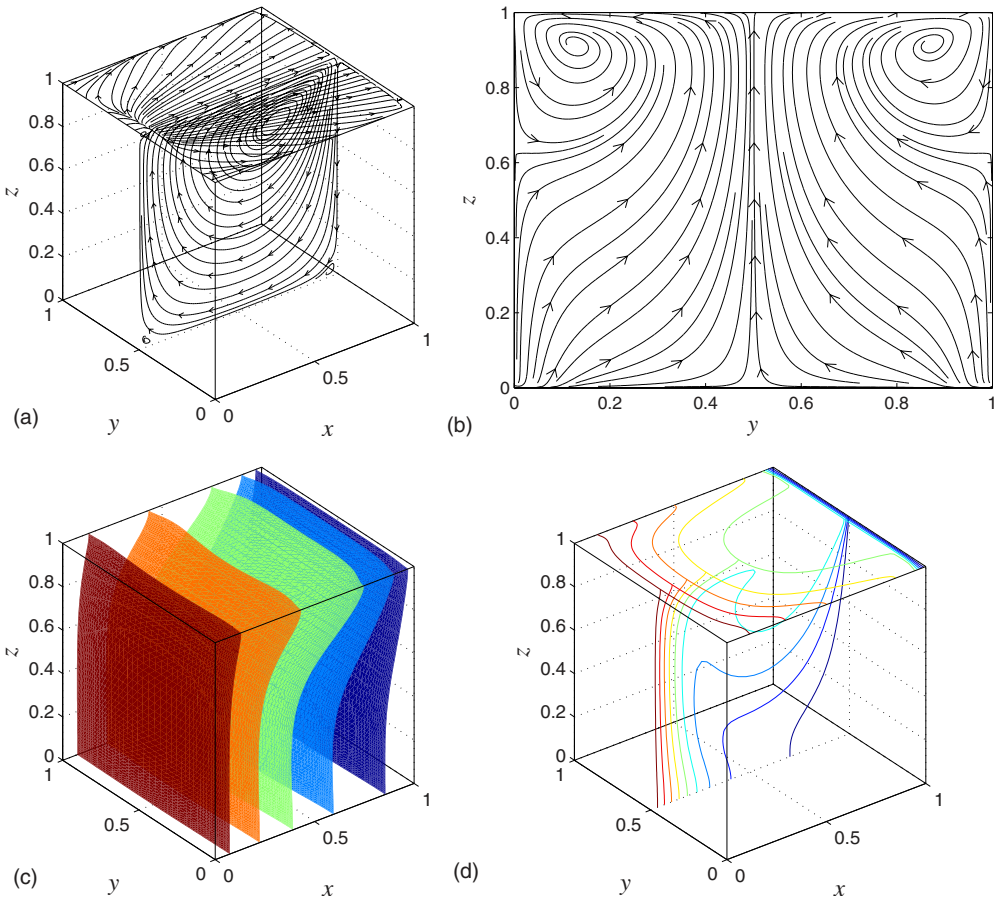

FIG. 4. (Color online) The same as Fig. 3 but for Re=120 and (d) presents contour slices, rather than isosurfaces, of the concentration field. The contour values in (d) are from 0.1 to 0.9 with steps of 0.1.

spatially and consists of four rolls. Such temporal chaotic dynamics is sometimes termed weakly turbulence since fully developed turbulence involves both temporal and spatial chaos. The present four-roll chaotic solution is very different from the two-roll asymmetric oscillatory solution presented in Fig. 7, which is obtained for exactly the same parameter (Re=400). We also tried meticulously by using very small step of Re to determine any possible four-roll oscillatory solution but failed. It seems that the dynamics is chaotic once the four-roll steady solution gets unstable.

When Re is further increased to 430 the dynamics undergoes a reverse transition from chaotic to steady flow and another steady solution branch in the range $430 \leq \mathrm{Re} \leq 475$ is obtained, as denoted by the hollow square and circle points connected by dotted lines in Fig. 2. The reverse transition with the increase in Re appears to be counterintuitive. Usually the expectation is that the dynamical behavior of the flow would become more and more complex as the Reynolds number is increased. The flow field for Re=450 is shown in Fig. 10. Back-front symmetry is regained and the secondary flow on the mid-y-z plane consists of three pairs of counter-rotating vortices. We refer to this solution as the six-roll symmetric solution. It is more efficient in heat and mass transfers than the two-roll asymmetric oscillatory flow coexisting in the same parameter range (Fig. 2). It is now apparent that the bifurcation to steady state also results in a change in the spatial structure to a more complex three-dimensional form. Thus, the apparently paradoxical reverse transition can now be reconciled within the existing dynamics theory. Essentially, the reduction in the temporal complexity (from chaotic to steady) is accompanied by an increase in the spatial complexity (from four rolls to six rolls). It can then be argued that the overall complexity increases after the bifurcation, so there is no paradox or anomaly. Another way to look at this reverse transition would be that the formation of the six-roll secondary flow stabilizes the chaotic behavior existing before the bifurcation. A real paradox would have arisen if it was found that the transition did not change the flow pattern and yet reverted to steady state, in which case our understanding of the transition phenomena would require revision. Similar reverse transition phenomenon, from two-frequency quasiperiodic to steady state, in three-dimensional Rayleigh-Bénard convection for small aspect ratio enclosure was also observed experimentally by Gollub and Benson [25] and later reproduced numerically by Mukutmoni and Yang [26].

When Re is further increased from 475 to 500 the dynamical behavior is again chaotic, as shown by the time signals of $u(0.5,0.5,1)$ and $v(0.5,0.5,1)$ in Fig. 11(a). Regular oscillations are interrupted from time to time by irregular noisy behavior (turbulent bursts). It seems that the flow is undergoing an intermittency route to chaos [25,27]. Again by correlation dimension calculation we obtain $d=2.84$, which gives the fractal dimension of the corresponding strange attractor of this chaotic regime. The snapshot of the flow field

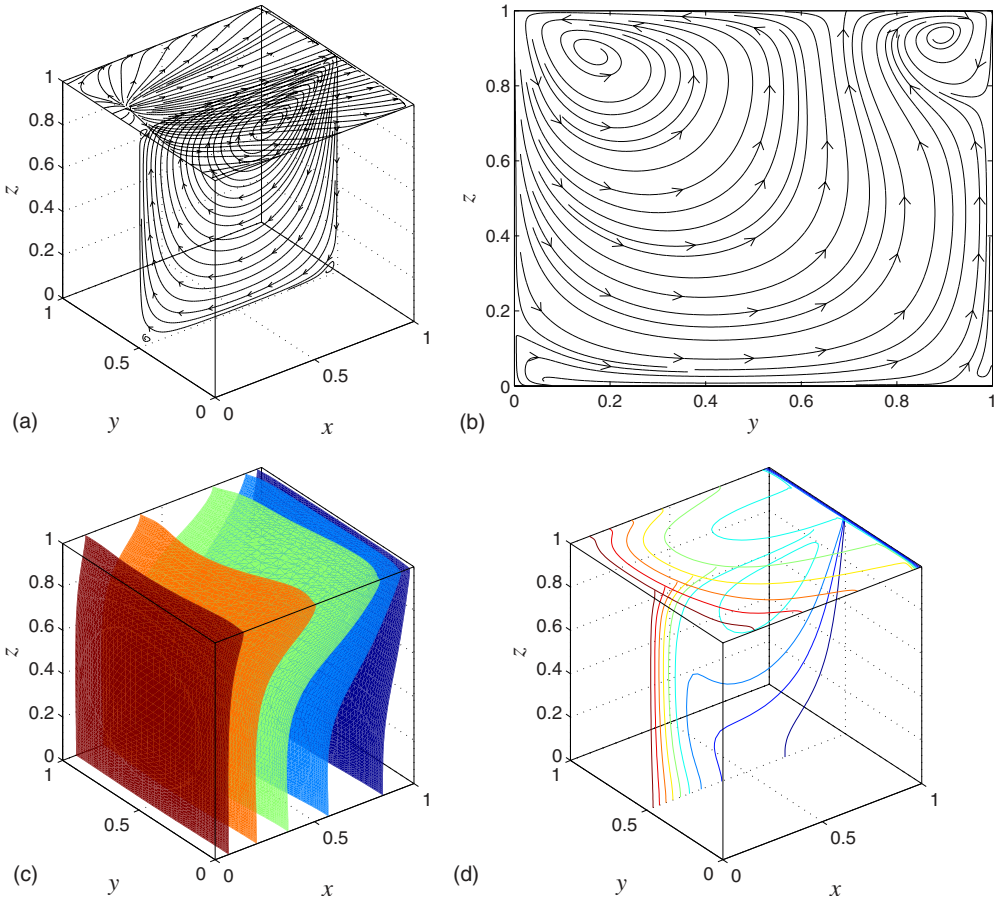

FIG. 5. (Color online) The same as Fig. 4 but for Re=200.

on the mid-y-z plane shows that the secondary flow still consists of six rolls [Fig. 11(b)].

2D model results are also presented in Fig. 2. It can be seen that the 2D model significantly overpredicts the heat and mass transfer rates. This suggests that the back and front sidewalls have some retarding or stabilizing effects on the main flow. However, due to the presence of these sidewalls, complex secondary flow (up to six rolls) forms and the solution becomes chaotic much earlier, in the sense of a smaller Re value. Thus, it can be seen that the effects of these sidewalls are quite complex. Totally seven dynamical behaviors, including two different chaotic regimes (Figs. 9 and 11), are observed up to the maximum Re value investigated, and thus

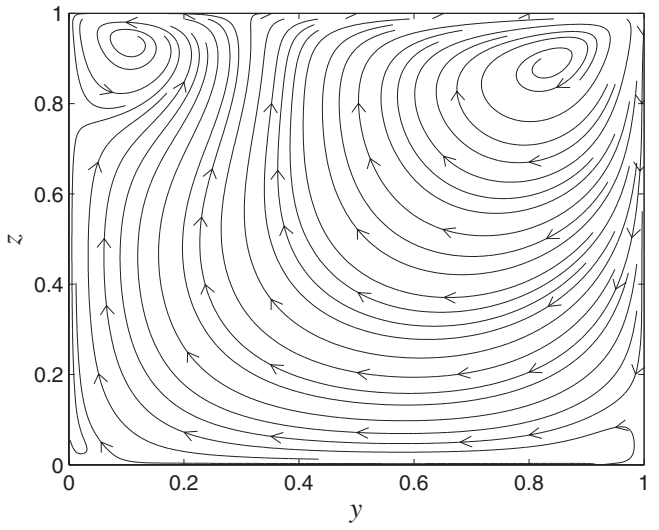

FIG. 6. Secondary flow on the mid-y-z plane for the same parameters as those in Fig. 5, showing another symmetry-breaking solution.

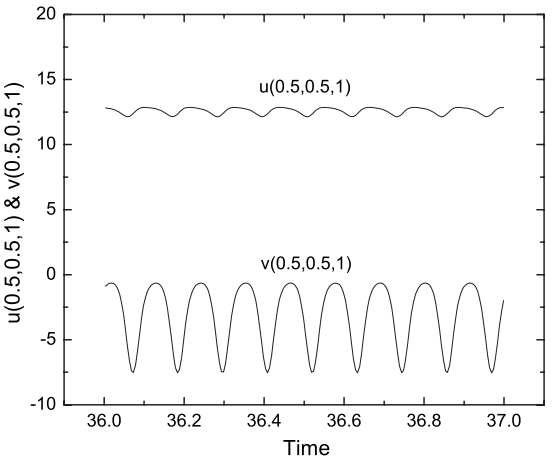

FIG. 7. Temporal responses of the horizontal velocity components at the center of the upper surface for Re=400, R_σ=−0.5, and Le=10.

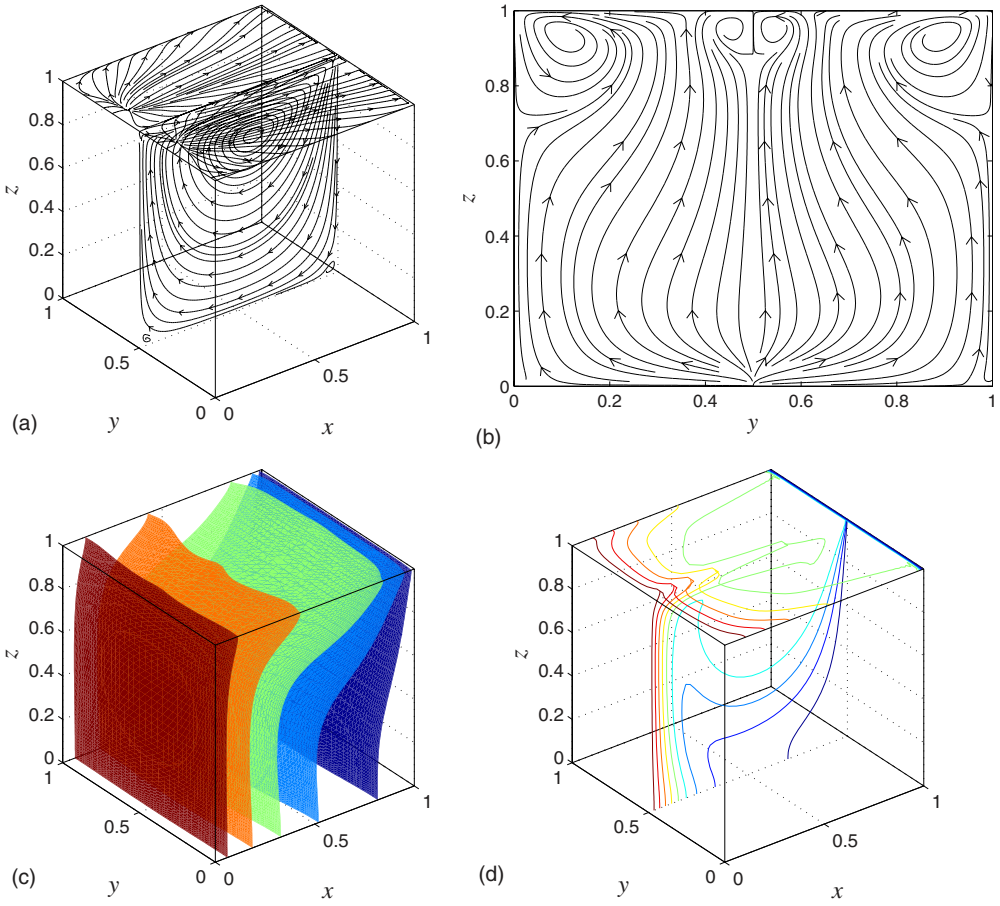

FIG. 8. (Color online) The same as Fig. 4 but for Re=340.

very rich dynamical behaviors will be missed when the 2D model is used.

B. Influence of R_σ

The influence of R_σ is studied for both opposing ($R_\sigma < 0$) and augmenting ($R_\sigma > 0$) flows, as shown in Fig. 12 for Re=200 and Le=10. Both 2D and 3D heat and mass transfer rates are shown and all the results represent steady flow results. The most important feature of this figure is that, in addition to the two-roll asymmetric solution (Fig. 5) in the range $-1 \le R_\sigma \le -0.5$ (square and circle points connected by solid lines), there coexists another symmetry-breaking solution branch in the range $-1 \le R_\sigma \le -0.6$ (square and circle points connected by dashed lines). The flow field of this second asymmetric solution is shown in Fig. 13 for R_σ=

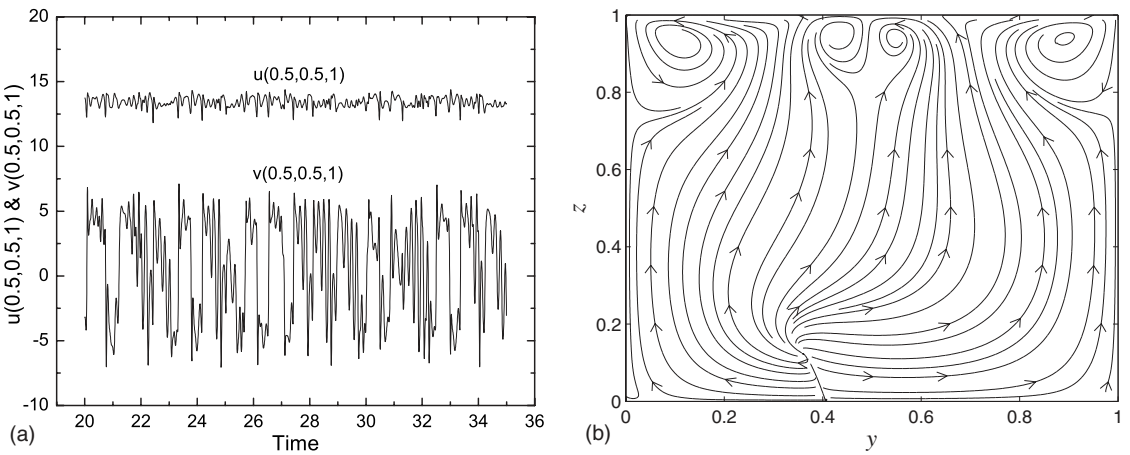

FIG. 9. (a) Temporal responses of horizontal velocity components and (b) snapshot of the flow field on the mid-y-z plane for Re=400, R_σ=−0.5, and Le=10.

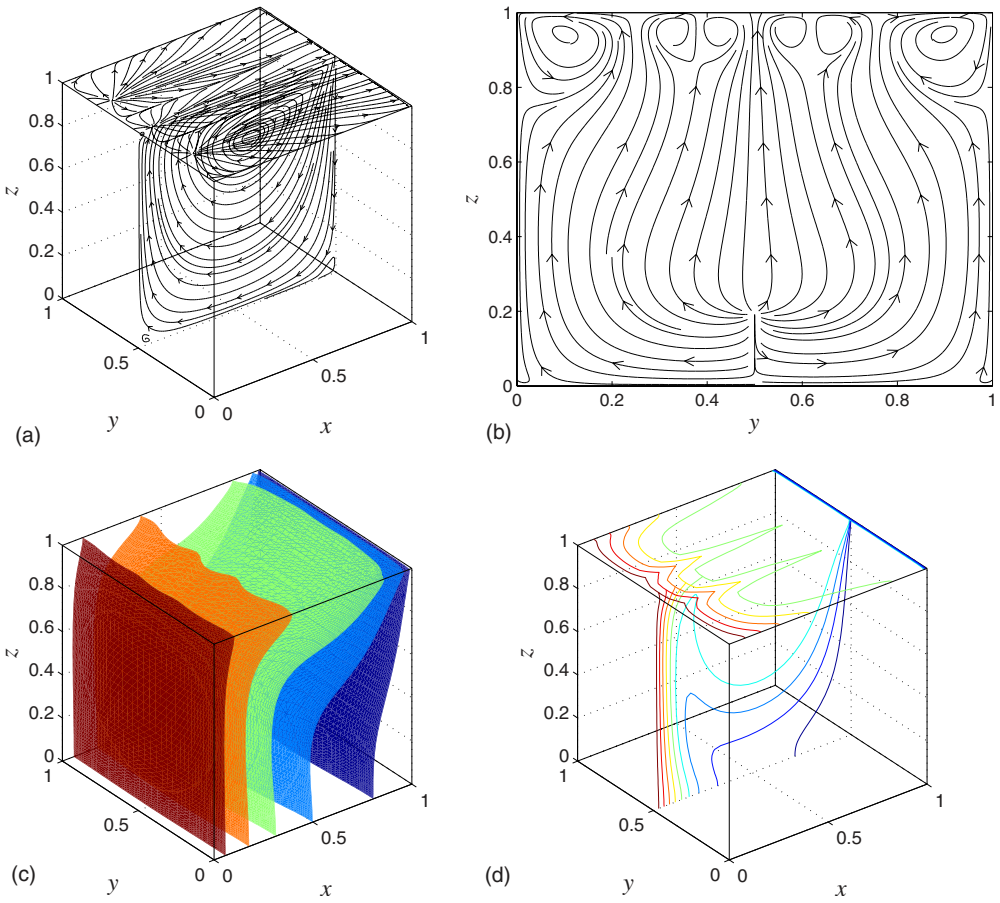

FIG. 10. (Color online) The same as Fig. 4 but for Re=450.

−0.8. As can be seen, the secondary flow on the mid-y-z plane consists of only one large vortex. This is different from the two-vortex structure of the first asymmetric solution (Fig. 5). The flow pattern on the upper surface [Fig. 13(a)] suggests that the secondary flow should be as strong as the primary flow (x-z plane), and this indicates that the flow is strictly three dimensional.

All the scattered square and circle points in Fig. 12 represent back-front symmetric solutions. The evolution of the secondary flow with R_σ is shown in Fig. 14. As can be seen, all the three opposing cases are qualitatively the same as the two-roll symmetric solution (Fig. 4), with two counter-rotating vortices circulating near the surface. As R_σ increases, the vortices near the surface disappear and two new counter-rotating vortices form in the lower half of the cavity. The transiting state with a four-vortex structure is shown at R_σ=0.1. Similar to Fig. 2, the 2D model overpredicts the heat and mass transfer rates in the range $-1.0 \le R_\sigma \le 1.0$,

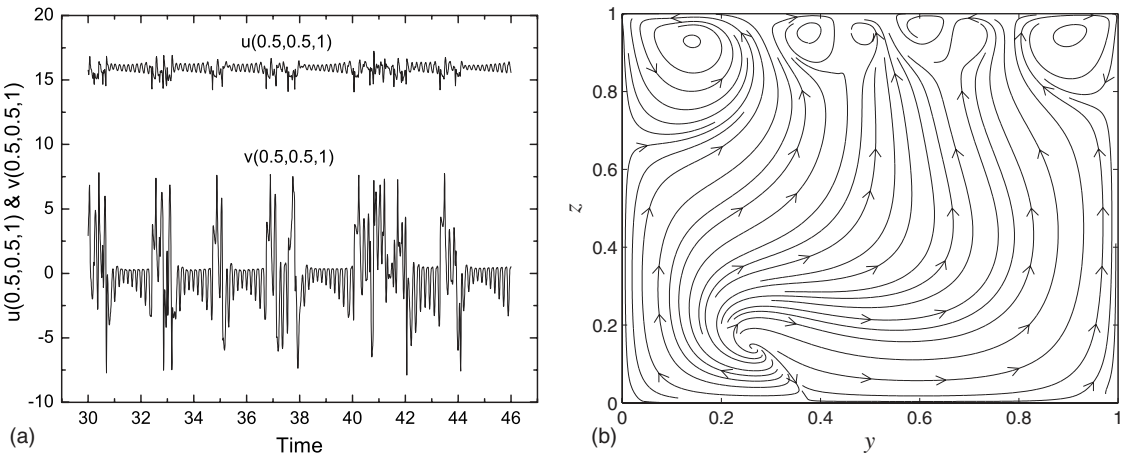

FIG. 11. (a) Temporal responses of horizontal velocity components and (b) snapshot of the flow field on the mid-y-z plane for Re =500, R_σ=−0.5, and Le=10.

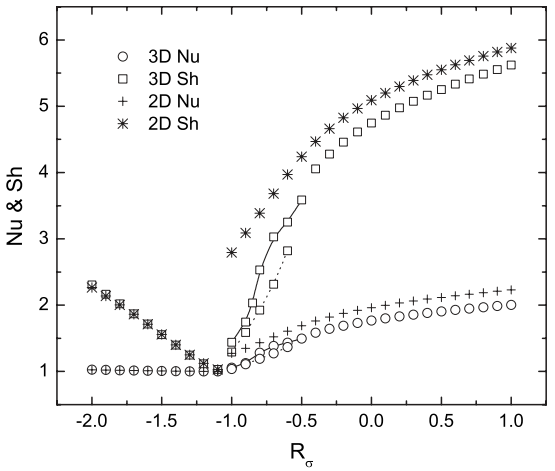

FIG. 12. Variations of Nu and Sh with R_σ for Re=200 and Le =10. The scattered square and circle points represent back-front symmetric solutions. The points connected by solid lines represent the two-roll asymmetric solutions (Fig. 5), while those connected by dashed lines represent another type of symmetry-breaking solutions (Fig. 13).

especially at $R_\sigma=-1$. But this is not the case in the range $-2.0 \le R_\sigma \le -1.1$, where the 2D and 3D predictions almost coincide. Although with the presence of the back and front sidewalls and the formation of the secondary flow, the 3D predictions do not differ much from the 2D predictions. The heat transfer rate in this range remains very close to that of the pure conduction state, while the mass transfer rate increases linearly with the increase in the opposing solutal Marangoni force.

When R_σ approaches -1 the flow intensity decreases, and thus the heat and mass transfer rates decrease. This is because at $R_\sigma=-1$ the thermal and solutal Marangoni forces are opposing and of equal magnitude. Actually such a condition would suggest a motionless equilibrium state. The onset of convection for this special case in a 2D cavity has been systematically investigated by Chen *et al.* [16], where it was shown that, due to small disturbances, the quiescent equilibrium loses stability via a supercritical Hopf bifurcation and near the bifurcation point there coexists a steady solution branch, which is induced by finite-amplitude disturbance. For the present cubical cavity the simultaneous existence of multiple solution branches is shown in Fig. 15 by plotting the maximum $u(0.5,0.5,1)$. The quiescent equilibrium solution encounters a primary Hopf bifurcation at H and then an oscillatory solution branch (branch 5) occurs. Linear stability analysis for the 2D case [16] predicts that the critical bifurcation point is located at $\mathrm{Re}_c=362$, while in the present 3D computations, by using a step of $\Delta\,\mathrm{Re}=10$, we determine that $\mathrm{Re}_c \approx 300$. A snapshot of the oscillatory flow near the onset of convection (Re=320) is shown in Fig. 16. Counter-rotating vortices travel from the right vertical wall to the left

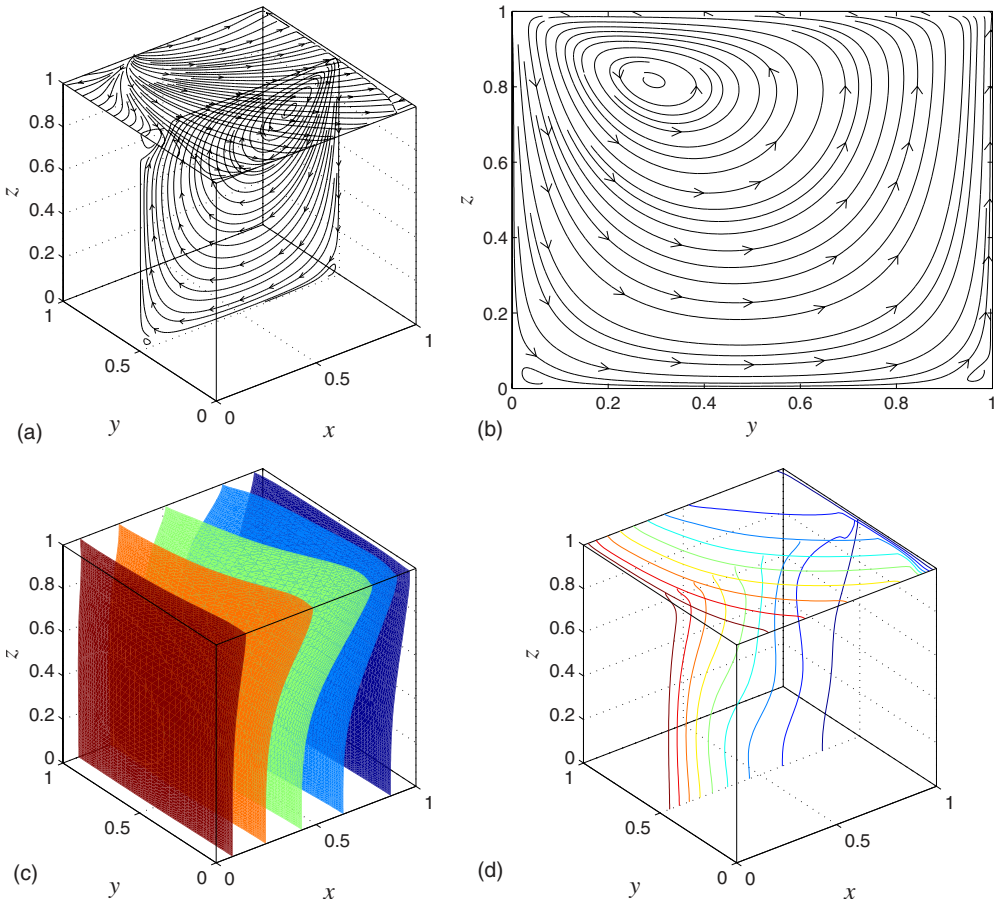

FIG. 13. (Color online) The same as Fig. 4 but for Re=200 and $R_\sigma=-0.8$.

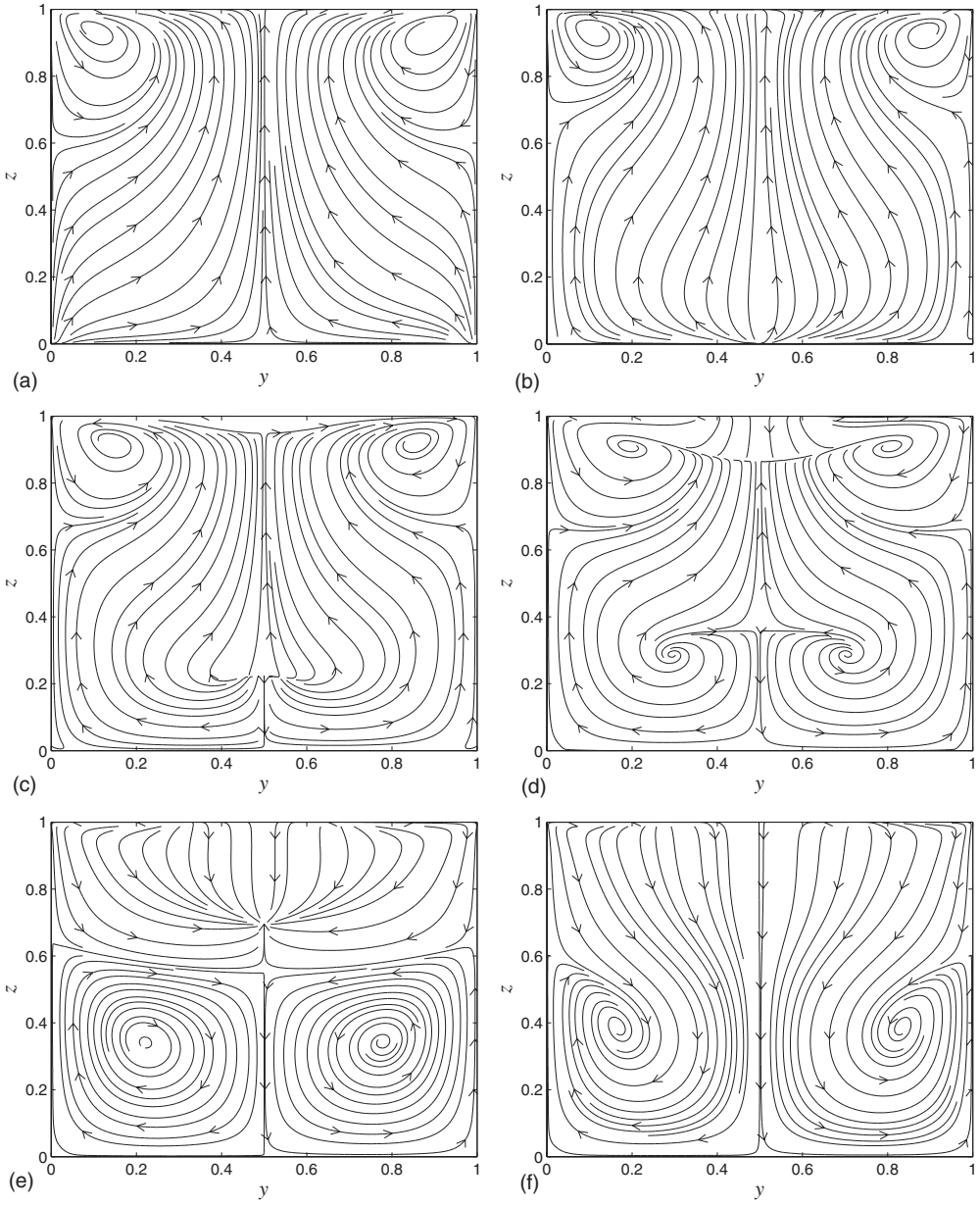

FIG. 14. Secondary flows on the mid-y-z plane for different R_σ values in Fig. 12: (a) $R_\sigma=-1.5$, (b) $R_\sigma=-0.4$, (c) $R_\sigma=-0.1$, (d) $R_\sigma=0.1$, (e) $R_\sigma=0.4$, and (f) $R_\sigma=0.8$.

vertical wall. The stream slice on the mid-x-z plane [Fig. 16(c)] shows that this is the mode II oscillatory flow identified by Chen *et al.* [16]. The flow patterns on the upper surface [Fig. 16(a)] and the mid-y-z plane [Fig. 16(b)] suggest that this oscillatory flow is back-front symmetric and basically two dimensional (flow in the y direction is almost vanishing). The temperature and concentration fields are almost identical, with the isotemperature and isoconcentration surfaces nearly parallel to the left and right vertical walls, and thus only the concentration field is plotted [Fig. 16(d)]. In Fig. 15 there also coexist two different steady asymmetric solution branches (branches 3 and 4) that are induced by finite-amplitude disturbances. While their x-component velocities at the center of the upper surface first decrease and then increase with Re, the corresponding y-component velocities both increase monotonically (not shown). It should be noted that branches 3 and 4, respectively, correspond to two different steady asymmetric solutions that are produced by a pitchfork bifurcation, e.g., branch 3 corresponds to the solutions shown in Figs. 5 and 6, which have exactly the same $u(0.5,0.5,1)$ value. Thus, near the primary bifurcation point there actually coexist five nontrivial solution branches: four steady asymmetric solutions plus one oscillatory symmetric solution. In the 2D case only one steady and one oscillatory solution coexist [16].

C. Influence of Le

The influence of Le on the heat and mass transfer rates is shown in Fig. 17 for Re=200 and $R_\sigma=-0.5$. Both 2D and 3D results are shown, and these all correspond to steady flow results. The square and circle points connected by solid lines

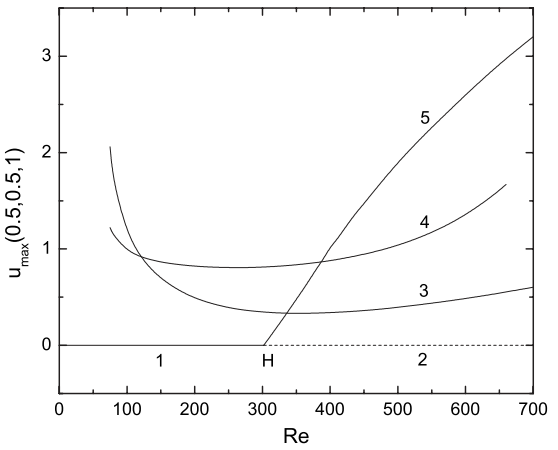

FIG. 15. The maximum $u(0.5,0.5,1)$ vs Re, showing multiple solution branches near the onset of convection for $R_\sigma=-1$ and Le $=10:1$, stable equilibrium solution; 2, unstable equilibrium solution; 3, steady asymmetric solution (Fig. 5); 4, steady asymmetric solution (Fig. 13); 5, oscillatory symmetric solution (Fig. 16). H denotes the supercritical Hopf bifurcation point.

represent the two-roll symmetric solutions (Fig. 4), while those scattered square and circle points represent the two-roll asymmetric solutions (Fig. 5). When Le is in the range $1<\mathrm{Le}<6$, the flow field is qualitatively the same as that shown in Fig. 4. When Le is increased from 6 to 7, a pitchfork bifurcation is encountered and the two-roll asymmetric solution is obtained. This further verifies the result in Sec. IV A that it is the presence of the slowly diffusing solute component that induces the pitchfork bifurcation. The heat transfer rate remains almost constant for large Le values, while the mass transfer rate keeps growing almost linearly in this log-log scale. For $\mathrm{Le}\leq 6$ the 2D model slightly overpredicts the mass transfer rate, while the overprediction becomes more significant when the 3D flow develops an asymmetric pattern. Finally, although different initial flow fields were used for starting the simulations, no additional solution branch could be identified in Fig. 17.

V. CONCLUSIONS

In the present work we attempt to model the three-dimensional aspects of double-diffusive Marangoni convection in a cubic cavity filled with a moderate Prandtl number fluid. Both the temperature and solute concentration gradients are applied horizontally. The direct numerical simulation procedure is carefully verified before being used. The main controlling parameters such as Re, R_σ, and Le are varied to gain new insights into the formation of different flow pat-

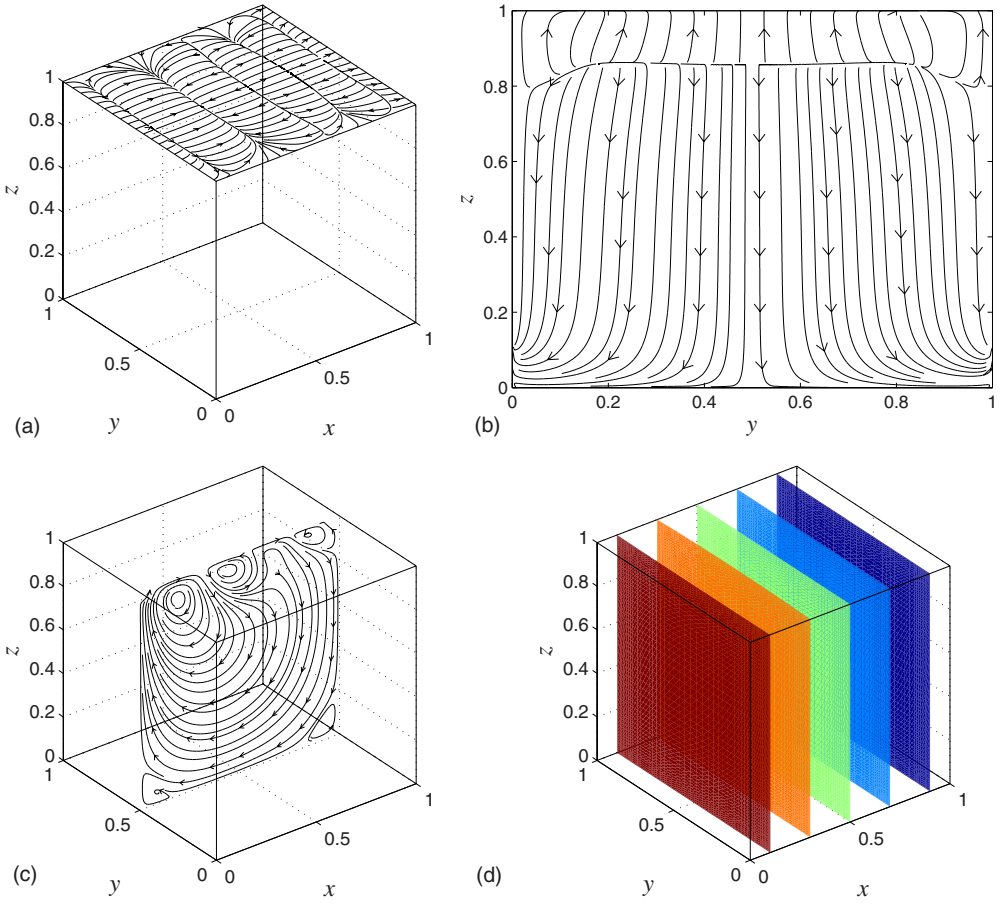

FIG. 16. (Color online) A snapshot of the oscillatory flow field for Re=320, $R_\sigma=-1$, and Le=10: (a) flow pattern on the upper surface, (b) stream slice on the mid-y-z plane, (c) stream slice on the mid-x-z plane, and (d) isosurfaces of the concentration field (contour values: 0.1, 0.3, 0.5, 0.7, and 0.9).

terns. Different initial flow fields were used in order to detect possible multiple solution branches.

The main findings of the present study can be summarized as follows: Upon increasing Re a two-roll symmetric secondary flow is first set up in the transverse (mid-y-z) plane, superimposed on the main flow rotation, which cannot be detected by the 2D model. A typical pitchfork bifurcation is encountered in the range $120 \leq \mathrm{Re} \leq 140$ and the back-front symmetry of the solution is lost. The resultant steady flow exhibits a two-roll asymmetric pattern on the transverse plane and a solute-rich fluid core develops below the upper surface. When Re is further increased from 380 to 400 the flow becomes oscillatory and a possible physical explanation is provided. In the range $260 \leq \mathrm{Re} \leq 380$ there coexists another solution branch, which corresponds to steady flows with a four-roll symmetric pattern on the transverse plane. It later becomes chaotic at Re=400 and a reverse transition from chaotic to steady flow is encountered when Re is further increased to 430. Examination of the transverse flow field shows that this counterintuitive reverse transition is accompanied by a change in the spatial structure from a four-roll to a six-roll pattern. The flow becomes chaotic once again at Re=500 and the temporal responses of the velocity components are characterized by intermittency. The presence of the back and front sidewalls can retard the main rotating flow and thus reduce the heat and mass transfer rates. However, the presence of such sidewalls gives rise to complex secondary flow (up to six rolls in the present study), which cannot be obtained by the 2D model. Totally seven dynamical behaviors, including two different chaotic regimes, are observed up to the maximum Re value investigated. Such rich dynamical behaviors would be missed if the 2D model is used.

For given values of Re and Le the influence of R_σ is investigated for both opposing and augmenting cases. Two different asymmetric solution branches are obtained in the range $-1 \leq R_\sigma \leq -0.6$, while for $R_\sigma < -1$ and $R_\sigma > -0.5$ the solutions are always back-front symmetric. While the 2D model significantly overpredicts the heat and mass transfer rates for $R_\sigma \geq -1$, the results by the 2D and 3D models almost coincide for $R_\sigma < -1$. When R_σ gets close to -1 both heat and mass transfer rates decrease due to the reduction in the convection intensity. The onset of convection for the special case $R_\sigma = -1$ is also investigated and the results are compared to the 2D analysis [16].

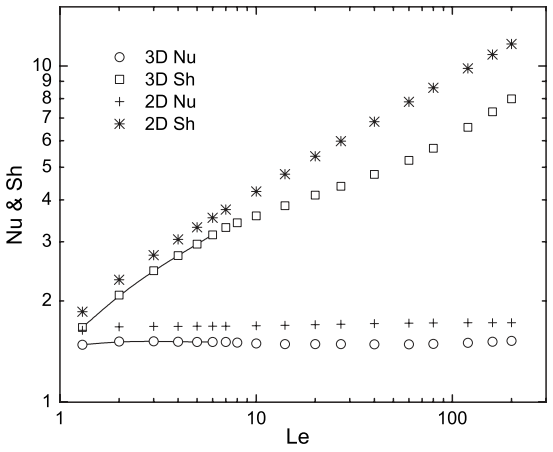

FIG. 17. Variations of Nu and Sh with Le for Re=200 and $R_\sigma = -0.5$. The square and circle points connected by solid lines represent the two-roll symmetric solutions (Fig. 4), while those scattered square and circle points represent the two-roll asymmetric solutions (Fig. 5).

As Le increases at fixed Re and R_σ a pitchfork bifurcation is encountered and the critical Le value is accurately determined. For different initial fields, all the simulations converge to the same solution and no additional solution branch was identified. The overpredictions of the heat and mass transfer rates by the 2D model are more significant for the asymmetric solutions than for the symmetric solutions.

The present study can be relevant in a zero or low gravity environment. However, we are aware that under normal gravity environment, for convection in a cube buoyancy effect should be important, and combined buoyant Marangoni flow is part of our further studies that are currently underway.

ACKNOWLEDGMENTS

The work described in this paper was supported by a grant from The Hong Kong Polytechnic University (Project No. G-U666) and the National Science Foundation of China (Grant No. 40476012).

[1] M. C. Cross and P. C. Hohenberg, Rev. Mod. Phys. **65**, 851 (1993).
[2] P. Colinet, J. C. Legros, and M. G. Velarde, *Nonlinear Dynamics of Surface-Tension-Driven Instabilities* (Wiley-VCH, Berlin, 2001).
[3] M. Lappa, Cryst. Res. Technol. **40**, 531 (2005).
[4] W. R. Wilcox, Prog. Cryst. Growth Charact. Mater. **26**, 153 (1993).
[5] Y. Kamotani, L. W. Wang, S. Ostrach, and H. D. Jiang, Int. J. Heat Mass Transfer **28**, 165 (1985).
[6] H. Han and T. H. Kuehn, Int. J. Heat Mass Transfer **34**, 449 (1991).
[7] H. Han and T. H. Kuehn, Int. J. Heat Mass Transfer **34**, 461 (1991).
[8] D. Gobin and R. Bennacer, Int. J. Heat Mass Transfer **39**, 2683 (1996).
[9] R. Krishnan, *ASME National Heat Transfer Conference, Philadelphia, 1989* (ASME, New York, 1989), p. 357.
[10] D. Gobin and R. Bennacer, Phys. Fluids **6**, 59 (1994).
[11] K. Ghorayeb and A. Mojtabi, Phys. Fluids **9**, 2339 (1997).
[12] S. H. Xin, P. Le Quere, and L. S. Tuckerman, Phys. Fluids **10**, 850 (1998).
[13] A. Bergeon, K. Ghorayeb, and A. Mojtabi, Phys. Fluids **11**, 549 (1999).

[14] Z.-W. Chen, J.-M. Zhan, Y.-S. Li, and Y.-H. Nie, Phys. Fluids **22**, 124101 (2010).
[15] T. L. Bergman, Phys. Fluids **29**, 2103 (1986).
[16] Z.-W. Chen, Y.-S. Li, and J.-M. Zhan, Phys. Fluids **22**, 034106 (2010).
[17] Y.-S. Li, Z.-W. Chen, and J.-M. Zhan, Int. J. Heat Mass Transfer **53**, 5223 (2010).
[18] I. Sezai and A. A. Mohamad, Phys. Fluids **12**, 2210 (2000).
[19] A. Bergeon and E. Knobloch, Phys. Fluids **14**, 3233 (2002).
[20] F. Verhaeghe, B. Blanpain, and P. Wollants, Phys. Rev. E **75**, 046705 (2007).
[21] A. Abidi, L. Kolsi, M. N. Borjini, H. Ben Aissia, and M. J. Safi, Numer. Heat Transfer, Part A **53**, 1357 (2008).
[22] J. H. Ferziger and M. Peric, *Computational Methods for Fluid Dynamics* (Springer-Verlag, Berlin, 2002).
[23] V. Saß, H. C. Kuhlmann, and H. J. Rath, Int. J. Heat Mass Transfer **39**, 603 (1996).
[24] P. Grassberger and I. Procaccia, Phys. Rev. Lett. **50**, 346 (1983).
[25] J. P. Gollub and S. V. Benson, J. Fluid Mech. **100**, 449 (1980).
[26] D. Mukutmoni and K. T. Yang, Int. J. Heat Mass Transfer **38**, 113 (1995).
[27] P. Berge, Y. Pomeau, and C. Vidal, *Order within Chaos: Towards a Deterministic Approach to Turbulence* (John Wiley & Sons, New York, 1984).